Materials and Design 160 (2018) 683–697

Contents lists available at ScienceDirect

Materials and Design

journal homepage: www.elsevier.com/locate/matdes

Combined modelling and miniaturised characterisation of high-temperature forging in a nickel-based superalloy

E. Alabort[a,c], R.C. Reed[b,c], D. Barba[b,c,*]

[a] Oxmet Technologies Ltd., 34 Centre for Innovation and Enterprise, Begbroke Science Park, OX5 1PF, United Kingdom
[b] Department of Engineering Science, University of Oxford, Parks Road, Oxford OX1 3PJ, United Kingdom
[c] Department of Materials, University of Oxford, Parks Road, Oxford OX1 3PH, United Kingdom

HIGHLIGHTS

- Uniaxial compression tests between 900–1100°C are used to elucidate the forging performance of the nickel superalloy IN903.
- A visco-plastic model with explicit microstructure dynamics is proposed and calibrated to our experimental observations.
- Forging simulators of double-cone experiments validate temperature, strain-rate and microstructure dependence of the model.
- The application of the framework is highlighted with an industry-relevant process model: the forging of a turbine disc.

GRAPHICAL ABSTRACT

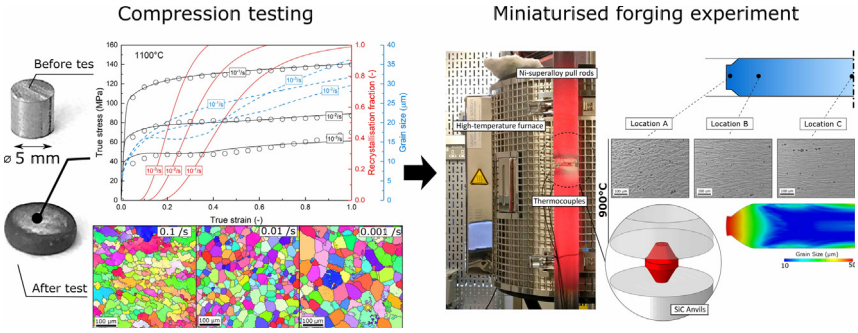

ARTICLE INFO

Article history:
Received 6 July 2018
Received in revised form 17 September 2018
Accepted 27 September 2018
Available online 2 October 2018

Keywords:
Superalloys
Forging
Process modelling
Continuum plasticity
Turbine discs

ABSTRACT

Continuum models and miniaturised experiments are used to elucidate the high-temperature forgeability of the Ni-based superalloy Inconel 903. Uniaxial compression high temperature tests allow the derivation of an apparent activation energy and the strain rate sensitivity of the deformation process, and to propose a unified constitutive model that captures the underlying physics of deformation. Metallographic analysis is then used to elucidate changes in microstructure which arise during the deformation process; microstructure evolution models which define the changes in grain size and recrystallisation during high temperature compression are proposed. Miniaturised forging experiments in double-cone specimens validate the modelling approach under relevant forging conditions at different temperatures and deformation rates. Finally, the deformation behaviour of this material in an industrially relevant manufacturing scenario – the forging process of a turbine disc – is studied numerically.

1. Introduction

Metals and alloys are often worked thermo-mechanically prior to their practical use in structural components. Why? The need to deform the material to an appropriate shape is one overarching reason for this [1-3]. But the prior use of some form of solidification processing – which is always required – is a also a significant factor; the mechanical properties, particularly in fatigue, are then enhanced greatly [4,5]. Moreover, the grain size is then reduced to values which confer substantial improvements in strength [6-8]. Examples of thermo-mechanical working include rolling, forming, stamping but also forging, of the type considered here.

* Corresponding author.
E-mail address: daniel.barba@materials.ox.ac.uk (D. Barba).

https://doi.org/10.1016/j.matdes.2018.09.048
0264-1275/

Table 1
Chemical composition for the Inconel 903 alloy investigated in this work (wt.%) obtained by EDX analysis.

Alloy	Ni	Co	Al	Ti	Nb	Fe
IN903	38.57	15.06	0.85	1.28	2.59	41.66

The above confirms that some measure of the rheological flow behaviour and its effect on underlying microstructure is required if processing is to be successfully optimised. During forging, materials are exposed to severe plasticity and high-temperatures which causes significant changes at the microstructure [9]; *i.e.,* dynamic and static recrystallisation, grain refinement, grain growth, and hardening-recovery due to dislocation accumulation [10-13]. Physically-based models with internal state variables (ISVs) are often used to model the evolution of these and their direct influence with the flow stress [14]. This is important because often these microstructural changes can make the deformation unstable — *e.g.,* with severe softening [15-17]. But more importantly, virtual knowledge of the as processed microstructure allows one to design forming processes that conform with the strict requirements of the gas turbine industry [18].

The research reported here was carried out with the above in mind. A combined experimental and modelling approach is proposed. First, uniaxial compression experiments at different temperatures and strain rates are used to elucidate and model the flow behaviour as a function of the underlying changes of microstructure. The alloy IN903 is employed as a vehicle to prove our methods. Based on experimentation, ISV that incorporate the effects of recrystallisation, dislocation accumulation and changes in grain size – both coarsening and refinement – are proposed. Then, a miniaturised forging framework is used to validate the rheological behaviour of a nickel-based superalloy. In the final part of this paper, the derived constitutive response is employed within an analysis of the closed-die forging process of a turbine disc to evaluate the influence of temperature and loading conditions on the flow response and microstructure.

2. Experimental methods

2.1. Material

The nickel-based superalloy Inconel 903 is studied in its polycrystalline form – its chemistry was measured using energy-dispersive X-ray spectroscopy EDS analysis and summarised in Table 1. This is a γ' strengthened alloy with approximately a 30% volume fraction present at room temperature. In this alloy, cobalt is present to improve the oxidation resistance, titanium, niobium and aluminium are added to promote hardening via the γ' precipitates. Its microstructural details can be found in elsewhere [19]. Fig. 1 shows an EBSD image of the initial microstructure together with the grain size distribution. This was obtained after casting and thermo-mechanical processing of an ingot prior to the mechanical testing carried out in this work. The microstructure can be summarised as distribution of large elongated grains surrounded by a population of equiaxed smaller grains.

2.2. Isothermal high-temperature compression testing — strain rate and temperature dependence of forging regime

Experimentation was carried out isothermally under constant displacement conditions. For this purpose, an Instron electro-mechanical testing machine (8862) was equipped with compression grips — see Fig. 2 (a). A conventional three-zone furnace was used to

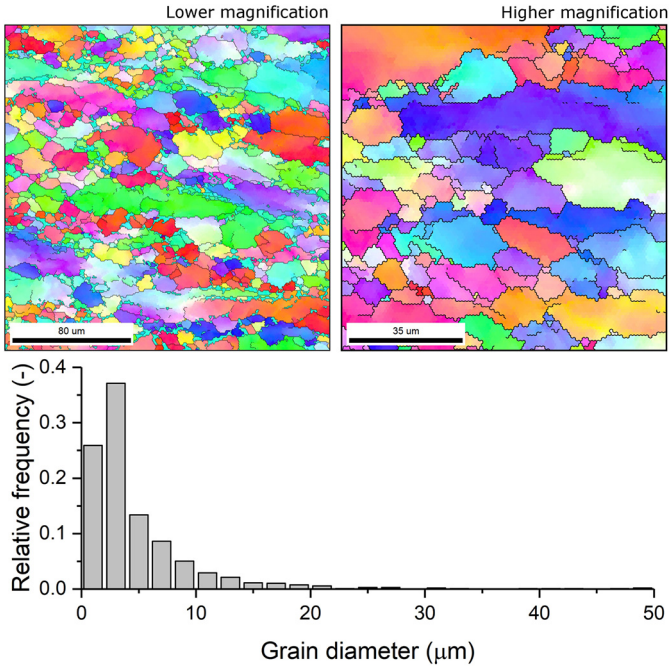

Fig. 1. Initial microstructure of the nickel superalloy used in the present study together with its grain size distribution.

guarantee the uniformity and control of the temperature. In-house pull-rods of approximately 6 mm in diameter were machined using nickel superalloy IN718. SiC disc anvils (50 mm diameter and 15 mm thick) were positioned at the end of the pull rods in the interface between sample-rod — these provided a very stiff hard surface and avoid indentation of the rod during testing. Compression tests were carried out at 100 °C increments between 900 and 1100 °C using constant strain rates of 0.1, 0.01, and 0.001/s. The defined testing conditions are believed relevant for the industrial exploitation of the forging process both in terms of temperatures and strain rates. Temperatures slightly above and below the expected solvus temperature were chosen to understand the impact of temperature and rate conditions under different forging regimes. Cylindrical samples measuring 5 mm in diameter and 5 mm in length (Fig. 2 (b)) were extracted from the thermo-mechanically worked billet using electron discharge machining (EDM). During the experiments, the temperature was monitored and feedback controlled using two thermocouples positioned inside the upper and lower pull rod, right next to the specimen gauge — see Fig. 2 (a). Tests were performed in air. The temperature of the furnace was ramped up at 10 °C/min and specimens were held for 15 min at the target temperature before straining commenced to ensure uniform temperature within the specimen. Right after testing, the furnace was split opened – without decreasing the temperature – and the sample was rapidly quenched in water.

2.3. Double-cone-cup compression testing — miniaturised compression forging

Isothermal, constant displacement rate miniaturised forging tests were carried out using the same machine and experimental set-up described above. Double-cone shaped compression specimens were used for this purpose. For the sake of validation, two different geometries were considered: (i) a tall double-cone specimen of an aspect ratio of ≈1.15 and (ii) a short one with an aspect ratio of ≈0.4. The

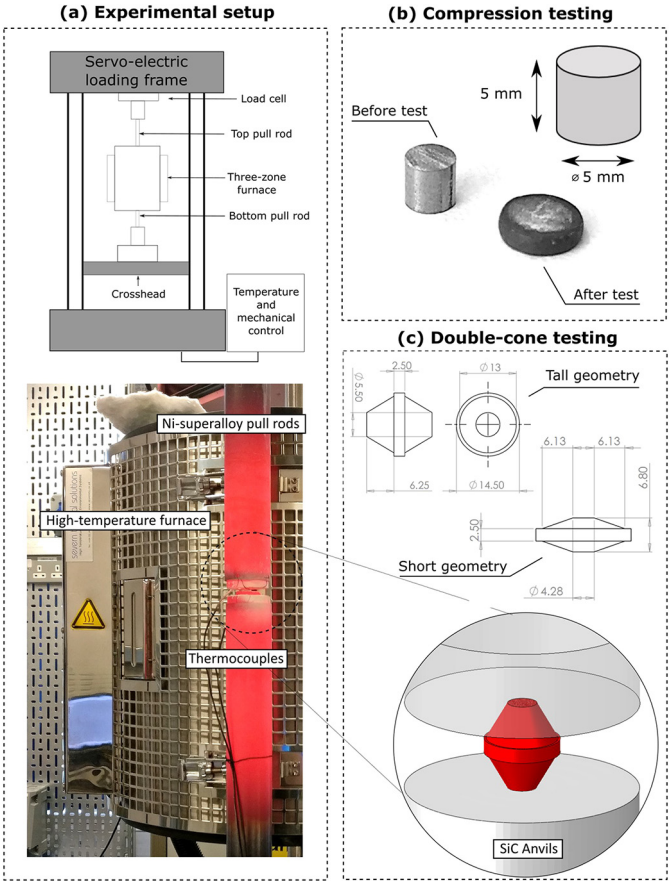

Fig. 2. a) Experimental set-up of the miniaturised forging experiment at high temperature; b) diagram of the miniaturised forging specimen; c) detail of the superalloy specimen set-up with SiC discs for transferring the load to the testing frame.

sample geometries are described in detail in Fig. 2 (c). Samples were cut from the same piece of material than the standard compression tests, maintaining the same orientation with respect to the original billet. Testing temperatures ranged from 900 to 1100 °C at 50 °C intervals between tests — 5 temperatures in total. The tall specimens were deformed at different displacement rates — 0.0015, 0.015 and 0.15 mm/s. The short geometries were forged at a displacement rate of 0.068 mm/s. As with the compression experiments, tests were performed in air and the specimens were held for 15 min to reach uniform temperature before straining commenced. Double-cone samples were also quenched in water right after the test completed.

3. Numerical methods

3.1. A constitutive model for high-temperature forging

A series of evolutionary equations – employing internal state variables – have been formulated to consider dynamic changes in the material during deformation. These equations consider the typical dynamic microstructural phenomena that occurs during forging such as hardening due to grain coarsening and softening due to dynamic recrystallisation and grain refinement at high temperatures [20].

The rate of viscoplastic flow is expressed in terms of steady-state creep strain rate $\dot{\varepsilon}_p$ as

$$\dot{\varepsilon}_p = \frac{A}{d^p} \exp\left\{\frac{-Q}{RT}\right\}\left(\frac{\sigma}{\sigma_0}\right)^n \tag{1}$$

where σ is the effective stress, Q is the apparent activation energy, R is the gas constant, T is the temperature, d is the grain size, A is a material constant also called the pre-exponential factor, σ_0 is the reference stress, and p and n are the grain size and stress exponents respectively.

3.1.1. Grain growth

Experimental studies have shown that during high temperature forming, static and dynamic grain growth are significant — particularly as the processing temperature increases [21]. This has a great influence on the mechanical behaviour of the alloy during deformation [22,23]. A kinematic grain size model which accounts for the effect of static grain growth $\dot{d}_{\text{static}}$ and dynamic grain growth $\dot{d}_{\text{dynamic}}$ has proposed following

$$\dot{d} = \dot{d}_{\text{static}} + \dot{d}_{\text{dynamic}} \tag{2}$$

where the static grain growth process is considered an atomic diffusion phenomenon affected by temperature and can be modelled following [24]

$$\dot{d}_{\text{static}} = \alpha_1 \exp\left\{\frac{-Q_{\text{st}}}{RT}\right\} d^{-\gamma_1}. \tag{3}$$

Here, α_1 and γ_1 are material constants, and Q_{st} is the activation energy of the static grain growth process. Dynamic grain growth is represented in the second term of Eq. (2) following [24] as

$$\dot{d}_{\text{dynamic}} = \alpha_2 \exp\left\{\frac{-Q_{\text{dn}}}{RT}\right\} \dot{\varepsilon_p} d^{-\gamma_2} \tag{4}$$

where α_2, γ_2 are material constants, and Q_{dn} is the activation energy of the dynamic grain growth process.

3.1.2. Dynamic recrystallisation

During high temperature deformation, continuous dynamic recrystallisation (dRX) is generally associated with the storage of dislocations that trigger nucleation of new grains [25]. When a critical dislocation density is reached, new grains with low dislocation density nucleate and grow — this process tends to generate equaixed microstructures. The effect of dislocation density on grain refinement was modelled following the works of Lin et al. [26] and Roy et al. [27]. The effect of grain refinement due to dynamic recrystallisation is accounted for by adding a third term to Eq. (2) which is expressed following

$$\dot{d}_{dRX} = -\alpha_3 \exp\left\{\frac{-Q_{\text{drx}}}{RT}\right\} \dot{X}^{\gamma_4} d^{\gamma_3} \tag{5}$$

where α_3, γ_3 and γ_4 are material constants, Q_{drx} is the activation energy of the dRX process, $\dot{X}$ is the dynamic recrystallisation rate and $\dot{S}$ is the rate of change of the volume fraction of recrystallised material. The dynamic recrystallisation rate $\dot{X}$ can be expressed as [28]

$$\dot{X} = \frac{x_0}{T} \exp\left\{\frac{-Q_x}{RT}\right\} \frac{\mu b^2}{2} \rho(\chi\varepsilon - \varepsilon_c(1-X))(1-X)^{x_1} \dot{\varepsilon}^{x_2} \tag{6}$$

where x_0, x_1 and x_2 are material constants, Q_x is the activation energy of recrystallisation, μ is the shear modulus, ε_c is the critical threshold strain at which dRX occurs and it is defined following [29] as $\varepsilon_c = 3.1 \times 10^{-4} Z^{0.16}$ where Z is the temperature dependent Zener-Hollomon parameter written as $Z = \dot{\varepsilon}\exp(-Q/RT)$. The shear modulus μ is approximated from [28] for IN718 as $\mu = 82.38 - 0.015\,T - 5.5 \times 10^{-6}\,T^2$. IN718 and IN903 has similar values of shear modulus above 600 °C [30] thus allowing for the use of this function for

IN903 in the temperature range studied here. Finally, the parameter χ is the onset grain incubation fraction defined by Lin et al. [26] and Bai et al. [23] as

$$\dot{\chi} = x_3 \exp\left\{\frac{-Q_\chi}{RT}\right\}(1-\chi)\rho \tag{7}$$

where x_3 is a material constant and Q_χ is the activation energy of the onset of recrystallisation.

The dislocation density rate was treated as an internal variable following the phenomenological model proposed by Mecking and Kocks [31]. In their model, the dislocation population accumulates as a function of plastic strain. At the same time, dynamic recovery processes such as rearrangement and annihilation reduce the density of dislocations. A number of models for the rate of dislocation density have arisen since then [10,22,32,33]. In the current work, the evolution of dislocation density $\dot{\rho}$ is expressed as [34]

$$\frac{d\rho}{d\varepsilon_p} = k_1\sqrt{\rho} - k_2\rho \tag{8}$$

where k_1 and k_2 are material constants. The parameter k_2 present a temperature dependency following Tang et al. [28] as $k_2 = k_{2t}\varepsilon^{-q}exp(-Q_k/RT)$ The first term in Eq. (8) represents the storage of dislocations as result of plastic straining. The second term models the reduction of dislocation density due to dynamic recovery. A third term is also introduced to account for the reduction of dislocation density due to recrystallisation following [22]

$$\dot{\rho} = -\frac{k_3(\rho-\rho_0)}{(1-X)^{k_4}}\dot{X} \tag{9}$$

where k_3 is a temperature-dependent material constant, X is the recrystallised fraction, and ρ_0 is the initial dislocation density ($1\times10^{12}/m^2$).

3.2. Optimisation of material constants

The introduced material constants were determined based on experimental data from the uniaxial compression high temperature tests. Global optimisation techniques were used – those minimise the error of a given objective function. In this study, a universal objective function was defined following [35]:

$$f(x) = f_\sigma + f_d \tag{10}$$

where f_σ and f_d are the residual error for stress and grain size respectively. Each of these residuals can be computed as function of model results and experimental measurements as

$$f_{\sigma,d,\xi} = \frac{1}{M}\sum_{j=1}^{M}\left(\frac{1}{N_j}\sum_{i=1}^{N_j} r_{\sigma,d}^2\right) \tag{11}$$

where N_j is the number of sampling points in each curve, M is the number of curves, and r is the distance between experimental and numerical points.

3.3. A unified time-dependent law for finite element analysis

The previously introduced creep law was implemented in a finite element model (FEM) to simulate the forging process. The viscoplastic laws were implemented in a finite strain framework. A common approach – which Abaqus/Standard [36] makes use of – is the additive decomposition of the stretch deformation rate tensor $\boldsymbol{D}$ as [37]

$$\boldsymbol{D} = \boldsymbol{D}^e + \boldsymbol{D}^p \tag{12}$$

where $\boldsymbol{D}^e$ and $\boldsymbol{D}^p$ are elastic and plastic components of the rate of stretch deformation respectively. This is a valid approach provided that elastic stretches are small ($\boldsymbol{V}^e \approx \boldsymbol{I}$), which is the usual assumption for plastic deformation of metals [38,39]. If so, one can determine the Jaumann (co-rotational) stress rate using linear elasticity as

$$\overset{o}{\boldsymbol{\sigma}} = 2G\boldsymbol{D}^e + \lambda \mathrm{Tr}\left(\boldsymbol{D}^e\right)\boldsymbol{I} \tag{13}$$

where G is the shear modulus and λ is the Lamé elasticity constant. This can be used to derive the material rate of stress following

$$\dot{\boldsymbol{\sigma}} = \overset{o}{\boldsymbol{\sigma}} + \boldsymbol{W}\boldsymbol{\sigma} - \boldsymbol{\sigma}\boldsymbol{W} \tag{14}$$

where $\boldsymbol{W}$ is the continuum spin tensor. Then, the Cauchy stress rate can be integrated over time in order to obtain the stresses within the material reference frame.

In order to implement the presented uniaxial constitutive relations in a FEM framework, it is necessary to generalise the constitutive laws for multiaxial conditions. Using the steady-state creep rate equation (Eq. (1)) and assuming Von Mises behaviour and the normality hypothesis, the multiaxial viscoplastic strain rate can be defined as [37]

$$\boldsymbol{D}^p = \frac{3}{2}\frac{\boldsymbol{\sigma}'}{\sigma_e}\dot{\varepsilon}_p \tag{15}$$

where σ_e is the effective stress, $\boldsymbol{\sigma}'$ is the deviatoric stress and $\dot{\varepsilon}_p$ is the effective plastic strain rate which follows from the set of equations introduced previously.

Using the stress rate tensor as defined in Eq. (14), it is possible to define the necessary stress update after a given increment of time as

$$\Delta\boldsymbol{\sigma} = \Delta\overset{o}{\boldsymbol{\sigma}} + (\boldsymbol{W}\boldsymbol{\sigma} - \boldsymbol{\sigma}\boldsymbol{W})\,\Delta t = \Delta\overset{o}{\boldsymbol{\sigma}} + \boldsymbol{R}\boldsymbol{\sigma}_t\boldsymbol{R}^T \tag{16}$$

where $\Delta\overset{o}{\boldsymbol{\sigma}}$ is the co-rotational stress increment assuming that $\boldsymbol{D}^e = \boldsymbol{D} - \boldsymbol{D}^p$. One should note that the stress provided by Abaqus at the beginning of the time increment has already been rotated and is $\boldsymbol{R}\boldsymbol{\sigma}_t\boldsymbol{R}^T$. These quantities can be updated within Abaqus using a UMAT or CREEP user-defined subroutines [36]. In the present work, the constitutive framework has been implemented in a CREEP subroutine.

4. Experimental results

4.1. Mechanical behaviour and the strain rate and temperature dependence of the forging regime

Results obtained using constant displacement compression tests of cylindrical coupons at temperatures relevant to the forging process were used to quantify the high-temperature formability of the alloy. Recorded force-displacement data was processed to obtain true stress-true strain curves — these are presented in Fig. 3. An image of the microstruture after the test is also presented for each of the experimental conditions. Fig. 4 presents the processed true stress-strain rate data for 2 different values of strain: 0.1 and 0.4 as obtained from Fig. 3. An analysis of the morphology of these curves is useful to identify the nature of the flow stress and its relationship to changes in the

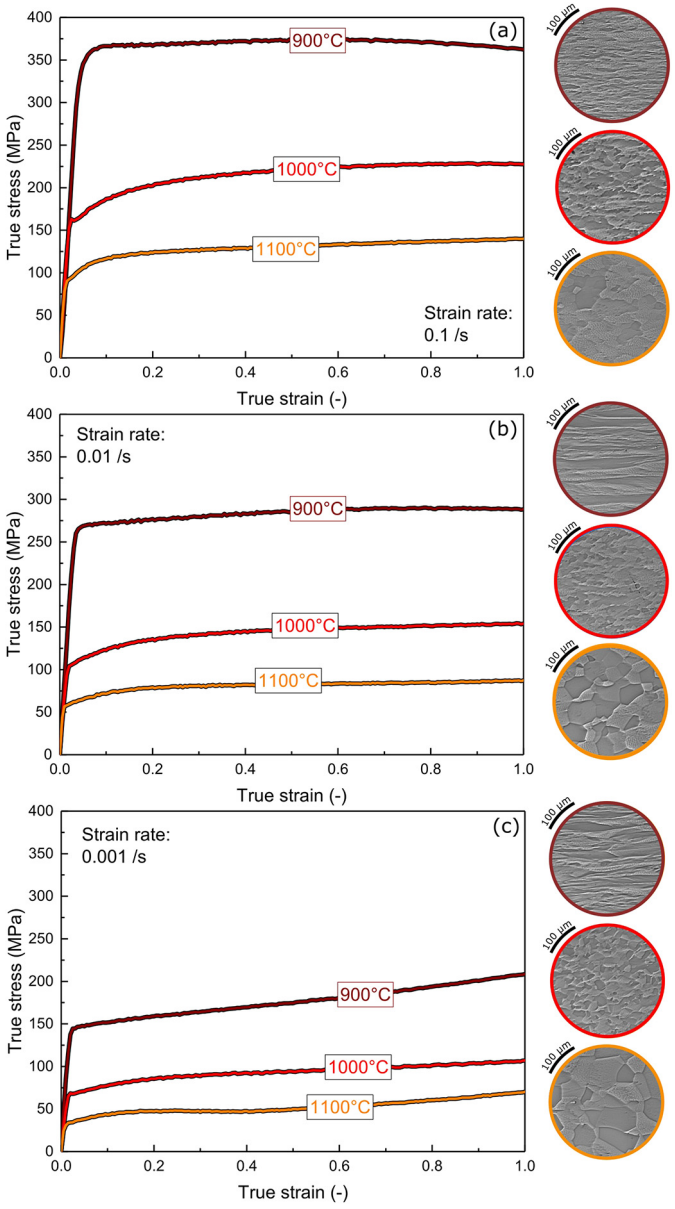

Fig. 3. Experimental stress-strain curves of IN903 alloy under different temperatures and strain-rates together with optical micrographs of the final microstructures for each of the testing conditions.

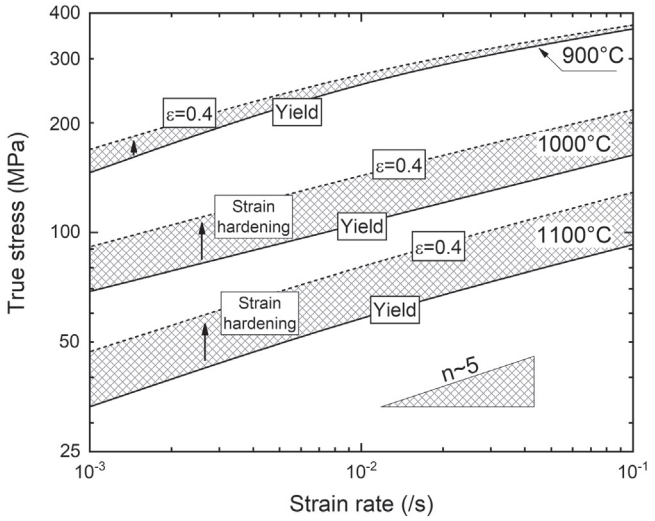

Fig. 4. Measured values of stress in IN903 during the compression tests as a function of the imposed strain-rate at different testing temperature. The shadow area represents the hardening experienced by the material as it undergoes plastic strain during the test.

microstructure. The following is observed; (i) At high strain rates ($\dot{\varepsilon} > 1 \times 10^{-2}$/s) and low temperatures (T < 950 °C) the curves show limited hardening and rather stable plastic flow. Changes in size and texture of grains are believed minimal — see micrographs in Fig. 3. (ii) At medium and high temperatures (T > 950 °C), only work hardening is reported. Such behaviour indicates that longer exposure at high temperatures is causing grain growth — this is also evident in the Fig. 3 micrographs. Recrystallisation is also likely to occur together with dynamic grain growth. Moreover, hardening tends to be more severe as the forming temperature increases.

The strain rate sensitivity parameter m— or its inverse the stress exponent n— can be expressed as function of logarithmic values of stress σ and strain rate $\dot{\varepsilon}$ given in Fig. 4 as $m = \frac{1}{n} = \left.\frac{\partial \ln \sigma}{\partial \ln \dot{\varepsilon}}\right|_{\varepsilon,T}$. A mean value of $n \approx 5$ is found. It is also observed that the value of n tends to decrease as the forming temperature increases and the strain rate decreases. A small value of n is indicative of an increase in the time dependency of the underlying mechanisms of deformation and it is associated to an increase in stability of the deformation process at the continuum scale that directly translates into the material being more formable.

Fig. 5 shows the temperature dependence of the stress for the different strain rates of interest. These curves can be used to calculate the apparent activation energy Q which can be estimated by the slope of the data when plotted as $\frac{1}{RT}$ vs $\ln\left(\frac{\dot{\varepsilon}}{A\,\sigma^n}\right)$. An apparent activation energy of approximately 550 kJ/mol is reported. The value of the apparent Q may shred light around the operative deformation mechanisms, but it also allows one to introduce the dependence of the temperature into a constitutive model.

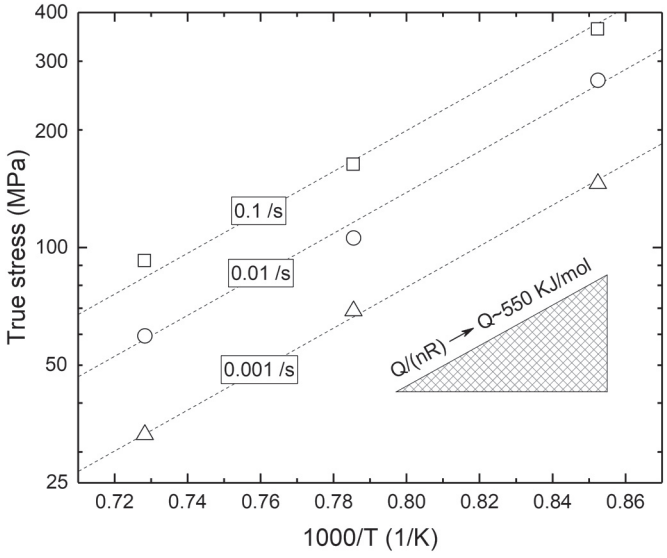

Fig. 5. True stress values as a function of the testing temperature for different strain-rate conditions measured in compression tests. The activation energy (Q) of the deformation mechanism in this range of temperature/stress is obtained from the linear fitting for each of constant strain rate conditions.

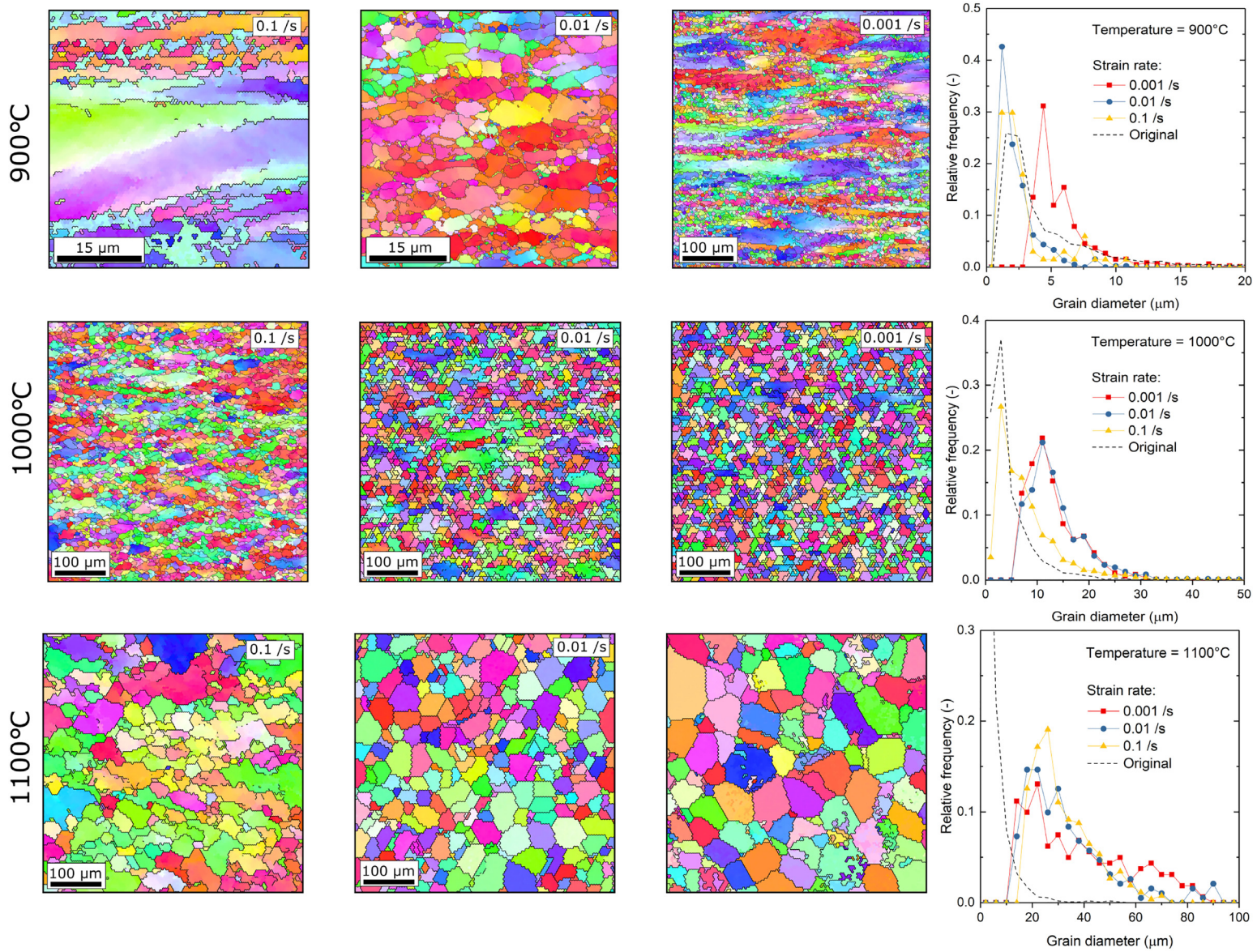

Fig. 6. EBSD inverse pole figures of the deformed microstructures of IN903 obtained after compression testing at different strain rates and T = 900 °C, T = 1000 °C and T = 1100 °C. The grain maps are processed to obtain the grain size frequency distribution for each of the testing conditions.

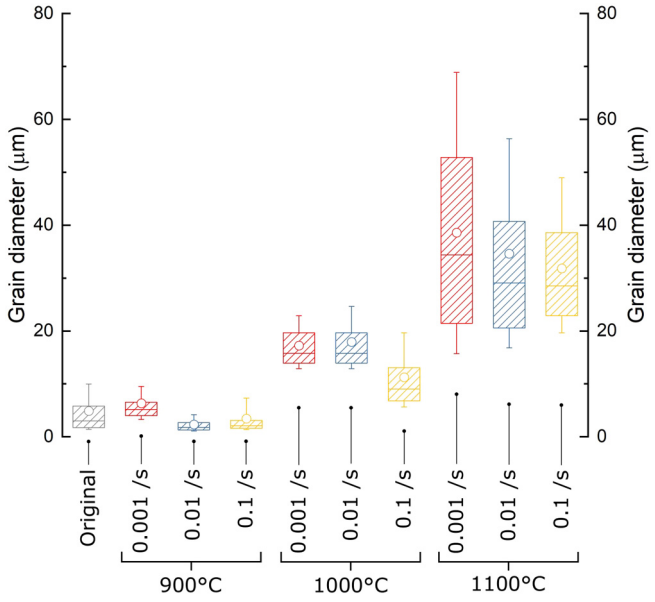

Fig. 7. Summary of the average grain size and variance measured for the whole set of temperatures and strain rates tested. Circle shows mean value, boxes indicate 25 and 75 percentile, box line shows the median, and whiskers shows the 10 and 90% values.

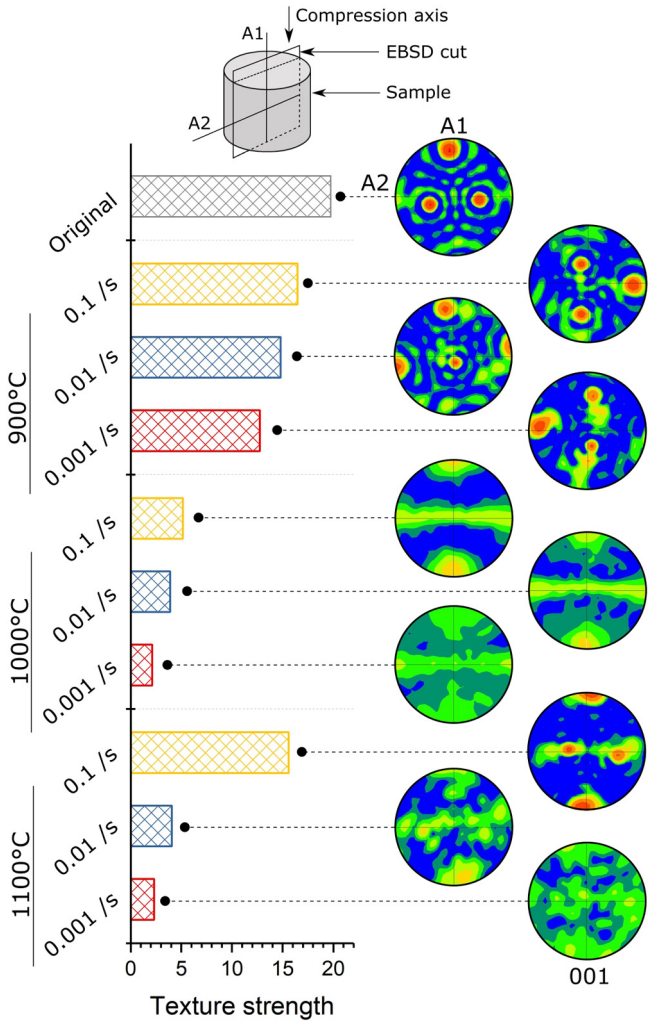

Fig. 8. Texture strength and texture pole figures after testing of IN903 for the different temperatures and strains rates conditions.

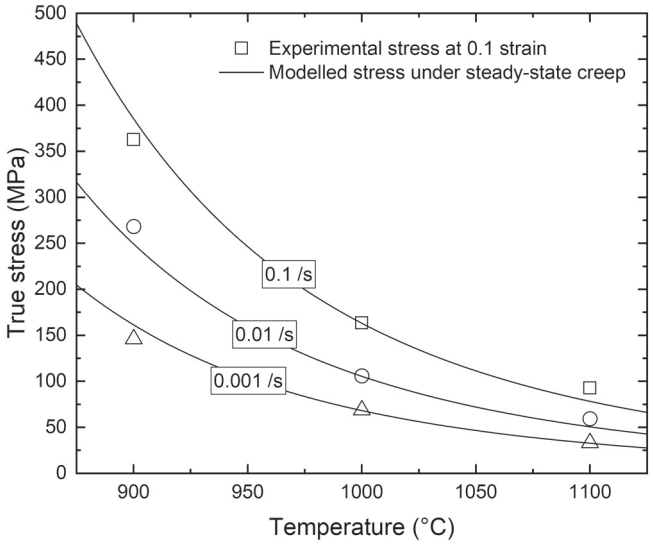

Fig. 9. Computed curves (continuous lines) and measured values (dots) of the true stress at 0.1 deformation as a function of the temperature for the different values of strain rates tested (0.1–0.001/s).

4.2. On the microstructural changes during the high-temperature forging

Experimental proof of the changes in microstructure which arise during high-temperature forging are presented here. Electron backscatter diffraction (EBSD) inverse pole figure maps and grain size distribution plots for samples deformed at 900, 1000 and 1100 °C are presented in Fig. 6. Grain growth is observed at almost every tested condition — except when deforming under faster strain rates and lower temperature when a decrease in the mean grain size is reported. Moreover, Fig. 7 summarises the grain size distribution of each condition — one may notice that the mean grain size tends to increase as the strain-rate decreases. However, the maximum and minimum grain size bands tend to tighten as the strain rate decreases. This potentially indicates that the recrystallisation process occurs at lower strains when the strain-rates are slower, thus obtaining a more homogeneous grain growth as the strain increases.

Inverse pole maps in Fig. 6 show fully recrystallised microstructures at 1000 and 1100 °C — grains are equiaxed, have increased

Table 2
Constitutive material parameters.

Steady-state creep law				
A (μm^{-1})	Q (J/mol)	σ_0 (MPa)	n	p
2.24×10^{11}	5.6×10^5	1	5.3	−1.5
Grain size dynamics				
α_1	γ_1	α_2	γ_2	α_3
1.25×10^8	1	1.75×10^{20}	2	1×10^{11}
γ_3	γ_4	Q_{st} (J/mol)	Q_{dn}	Q_{drx}
0.5	1	2.2×10^5	4.1×10^5	3.2×10^5
Dislocation dynamics				
k_1	k_{2t}	q	Q_k (J/mol)	k_3
5×10^8	1.35×10^4	0.17	6.2×10^4	6.94
Recrystallisation dynamics [28]				
x_0	x_1	x_2	x_3	b (m^2)
2.1×10^9	8×10^{18}	0.305	0.37	2.54×10^{-10}
k_4	Q_x (J/mol)	Q_χ (J/mol)		
1.925	3.7×10^5	4.8×10^5		

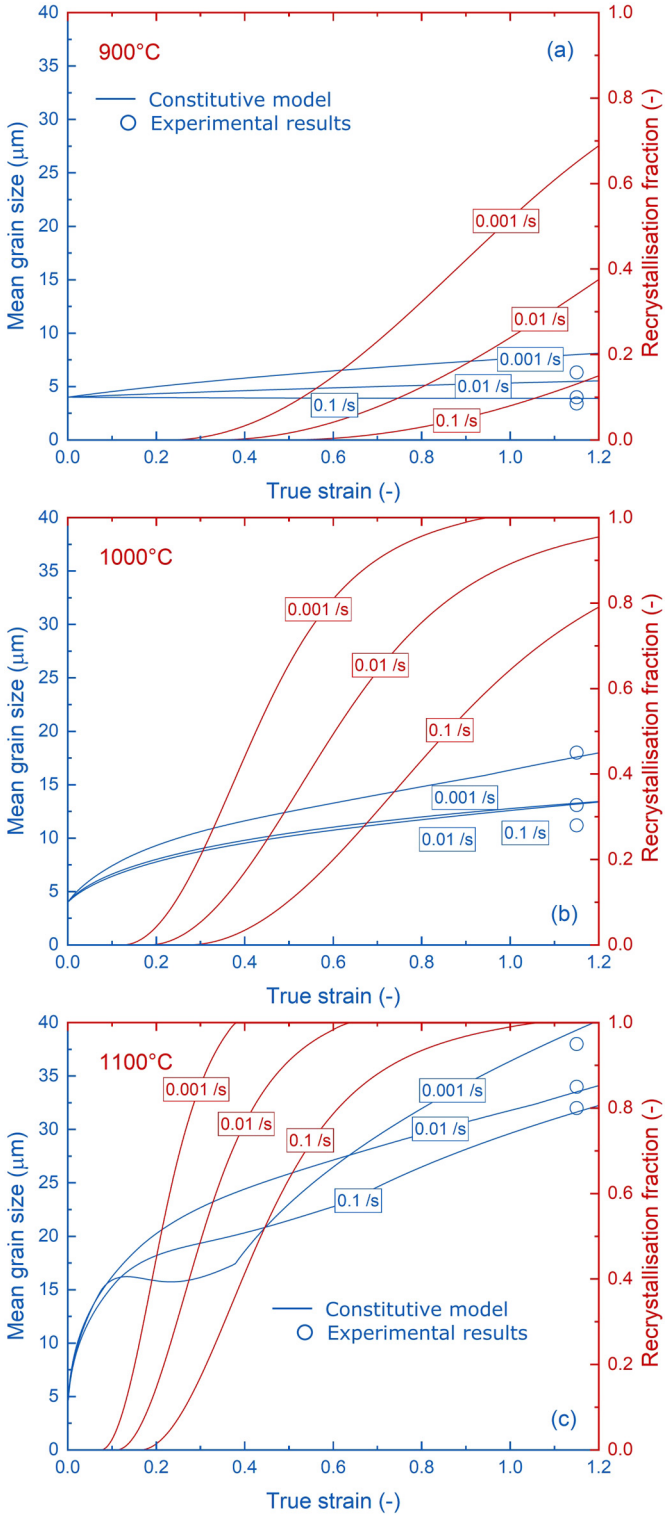

Fig. 10. Evolution of the mean grain size and recrystallisation fraction as a function of the testing strain obtained from the constitutive model (continuous lines) for the different temperatures and strain rate conditions. Experimental values of the mean grain size measured experimentally at the end of the tests are shown as dot points.

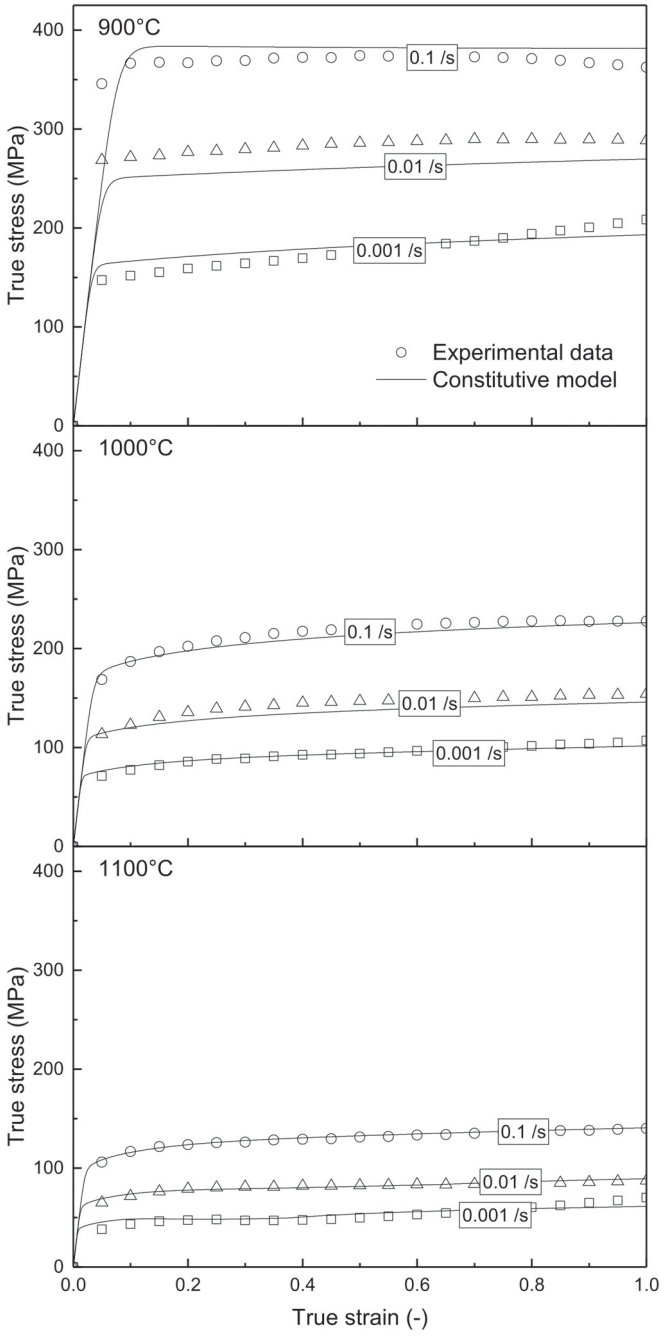

Fig. 11. True-stress against true-strain curves computed from the constitutive model (continuous lines) compared with the experimental ones (dot points) for the different temperature and strain rate conditions.

in size, and show little intragranular lattice distortion. This can be indicative of a large amount of activity at the grain boundaries — *e.g.*, grain boundary sliding. Maps for the case of 900 °C are different: those have elongated grains with evident amount of lattice distortion (indicative of large amount of plastic strain) surrounded by very small grains at the grain boundaries (please note the smaller scale of the two top images in Fig. 6). This is indicative of a partially recrystallised microstructure at the grain boundaries.

Fig. 8 shows the texture at the end of the compression test for each specimen. For all tested conditions, the randomness of the crystal orientation increases, thus the texture weakens as the forging strain accumulates. This effect supports the claim that recrystallisation together with some short of grain boundary activity at high temperatures is the main deformation mechanism. Moreover, the texture at 900 °C shows little texture reduction when compared to the original texture. This supports the hypothesis that only partial

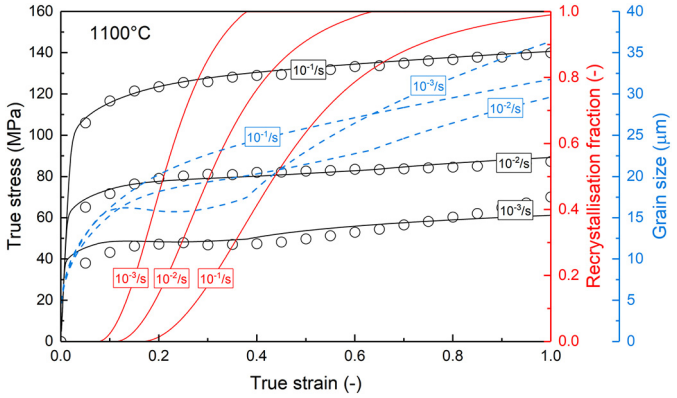

Fig. 12. True-stress against true-strain curves for the tests performed at 1100 °C and their associated grain size and recrystallisation fraction evolution. The clear effect of the recrystallisation and grain growth competition on the inhibition of the hardening for low strain rates (10^{-3}/s) is observed.

recrystallisation occurs at that temperature — slightly larger at the slowest strain-rate. These observations will be used later to calibrate the recrystallisation equations of our constitutive model.

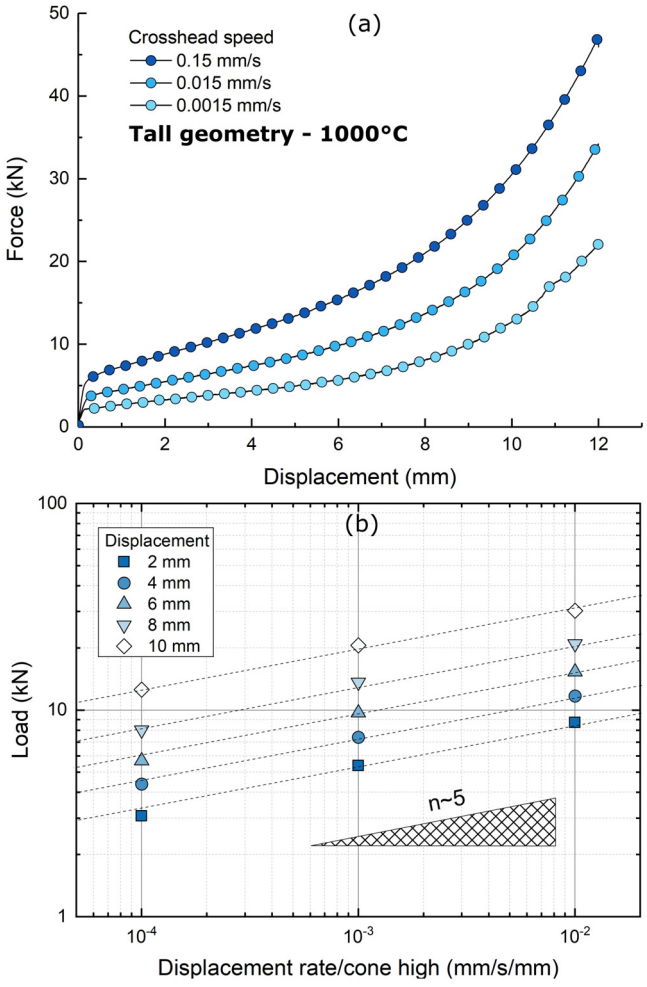

Fig. 13. a) Experimental curves of the cross-head force vs. displacement of the miniaturised forging experiment using the high aspect-ratio double-cone specimens for different values of displacement rates between 0.15 and 0.0015 mm/s and constant testing temperature; b) measured load values at different displacement points during the tests as a function of the non-dimensional displacement rate.

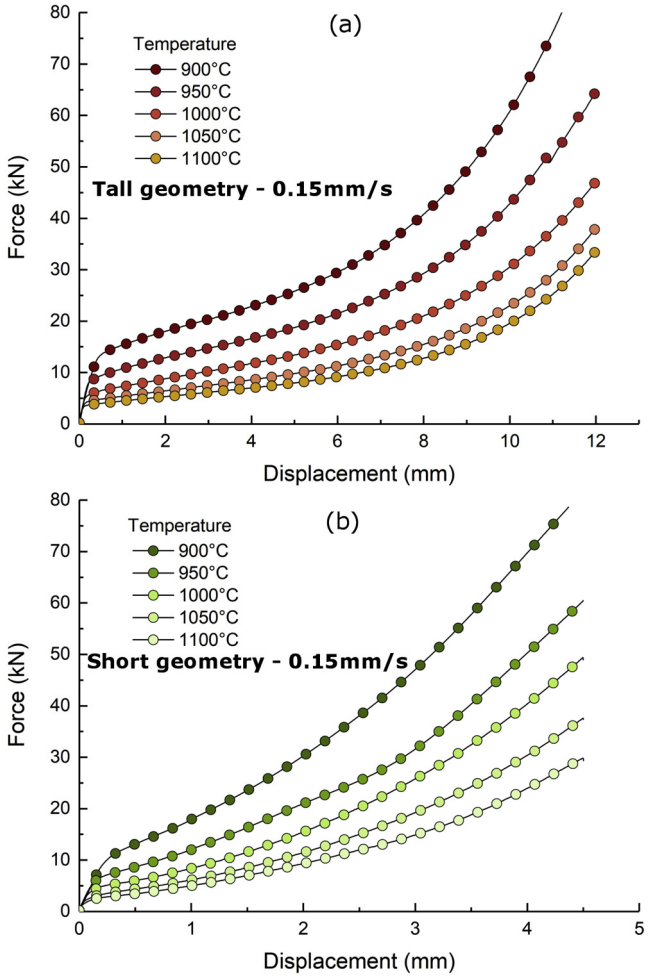

Fig. 14. Experimental curves of the cross-head force vs. displacement of the miniaturised forging experiment for different values of temperature between 900 and 1000 °C and constant displacement rate of 0.15 mm/s; a) for the high aspect-ratio double cone specimens and b) for the low aspect-ratio specimens.

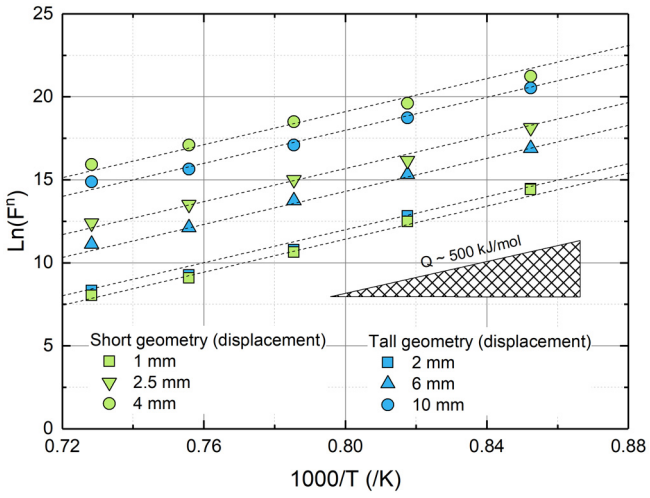

Fig. 15. Experimental cross-head forces vs. testing temperature for a constant displacement rate of 0.15 mm/s at different displacement values: 2, 6 and 10 mm. The fitted slope of the three different curves represents the apparent activation energy of the deformation process during forging.

4.3. Determination of material parameters for constitutive law

In this subsection, the values of the material parameters present in the constitutive equations are determined from experimental measurements. A two-step optimisation path is used. During the first optimisation step – where no microstructural changes are expected at very low strains – only the yield strength and its dependence with strain rate and temperature is considered. The initial values of the stress exponent n and the apparent activation energy Q are taken from Figs. 4 and 5 respectively. The computed stresses shown in Fig. 9 are obtained after the optimisation of parameters A, n, and Q — summarised in the top part of Table 2. This shows that the model is able to capture the initial strength as function of temperature and strain rate. However, strain dependent phenomena such as hardening and softening cannot be captured with a steady-state model.

As described previously, changes in grain size are introduced in terms of grain growth and grain refinement respectively. The calculated mean grain size at temperatures of 900, 1000 and 1100 °C and strain rate values between 10^{-3} and 10^{-1}/s presented in Fig. 10 are used to inform the model. The mean grain size data presented as scatter points in Fig. 10 is used for the determination of parameters α_1, α_2, α_3, γ_1, γ_2, γ_3, γ_4, Q_{st}, Q_{dn} and Q_{drx}. Solid lines in Fig. 10 represent the computed values of grain size for each temperature and strain rate together with the predicted recrystallisation kinetics. Dislocation and recrystallisation parameters k_1, k_{2t}, k_3, q, Q_k, x_0, x_1, x_2, x_3, b, k_4, Q_x and Q_χ were based on the model proposed by Tang et al. [28]. The optimised parameters for evolution of the grain size and the dislocation density are shown in Table 2. The computed stress-strain curves are presented with solid lines in Fig. 11 along with experimental values. The model shows good agreement and successfully links hardening and softening to changes in the mean grain size exclusively. More particularly, Fig. 12 shows how successfully modelling the grain size evolution allows one to capture the full strain-path of the forging process – this highlights the importance of modelling the competition between grain growth and recrystallisation for different strain rates and their effect on the forming stress.

5. Validation and application

In this section, in order to illustrate the advantages and the power of our approach, the model was first validated against simulated forgings employing double-cone experimentation. Then, the modelling framework was used to simulate the forging process of an aerospace turbine disc.

5.1. Effect of deformation rate on forging behaviour

A series of miniaturised forging experiments were carried out at different displacement rates and temperatures to study the underlying deformation mechanisms taking place during forming — the same information will be later used to validate the computational model in a more relevant forming scenario. During these miniaturised forgings, the displacement was halted if a maximum load of 80 kN was reached or if the maximum displacement was achieved: 12 mm for the tall double-cone geometry and 4 mm for the short geometry. First, the strain rate sensitivity is measured and compared to that measured using uniaxial compression tests. For this purpose, double-cone experiments at the same temperature but different deformation rates were carried out. Fig. 13 shows the behaviour of the tall double-cone specimens when formed at three different displacement rates (0.15, 0.015, and 0.0015 mm/s) at an isothermal temperature of 1000 °C. There is a noticeable influence of the deformation rate on the measured loads, these increase as the speed of forging increases. The shape of the curve can be divided in three zones: (i) a steep increase of load with displacement as the specimen is loaded elastically, (ii) a flattened region — where creep-like plasticity is activated, and (iii) a quick increase of load due to the rapid increase of effective cross-section of the sample as the forging process gets closer to completion.

In the first instance, the regime of deformation is compared to uniaxial compression tests by deducing the homogenised stress exponent n using the data shown in Fig. 13. This exponent was defined previously as $n = \left.\frac{\partial \ln \dot{\varepsilon}}{\partial \ln \sigma}\right|_{\varepsilon,T}$. Since we are comparing the slope

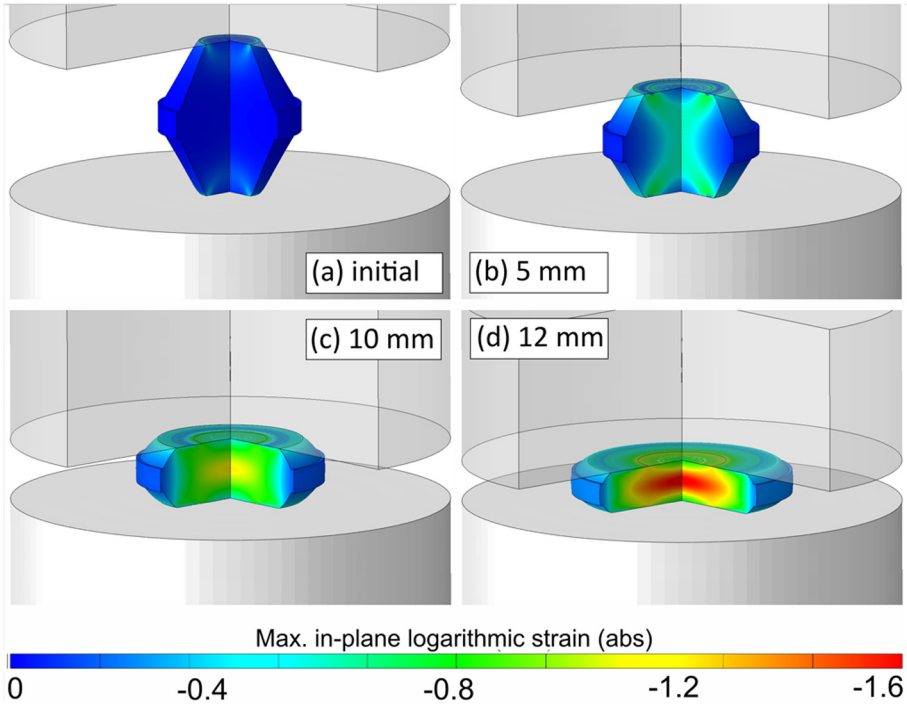

Fig. 16. Computational modelling of the miniaturised forging test (high aspect-ratio specimen). The maximum logarithmic strain is shown for (i) initial state, (ii) 5 mm deformation, (iii) 10 mm deformation and (iv) 12 mm deformation or final state.

at equal displacement points – but different displacement rates – the homogenised values of stress and strain rates can be written as $\dot{\varepsilon} = \dot{s}/h$ and $\sigma_i = F/A_i$ where $\dot{s}$ is the displacement rate, h is the height of the sample, F is the load, σ_i is the stress, and A_i is the sample effective area for the *ith* deformation point. Since the deformation points are well established for each deformation rate, the effective area is indeed a constant and does not affect the derivation of the slope — thus vertical axis of Fig. 13 is showing load instead of stress. Following this procedure, one obtains a stress exponent of $n \approx 5$ — this is consistent with the value measured using isothermal compression tests and provides confidence on the miniaturised forging procedure.

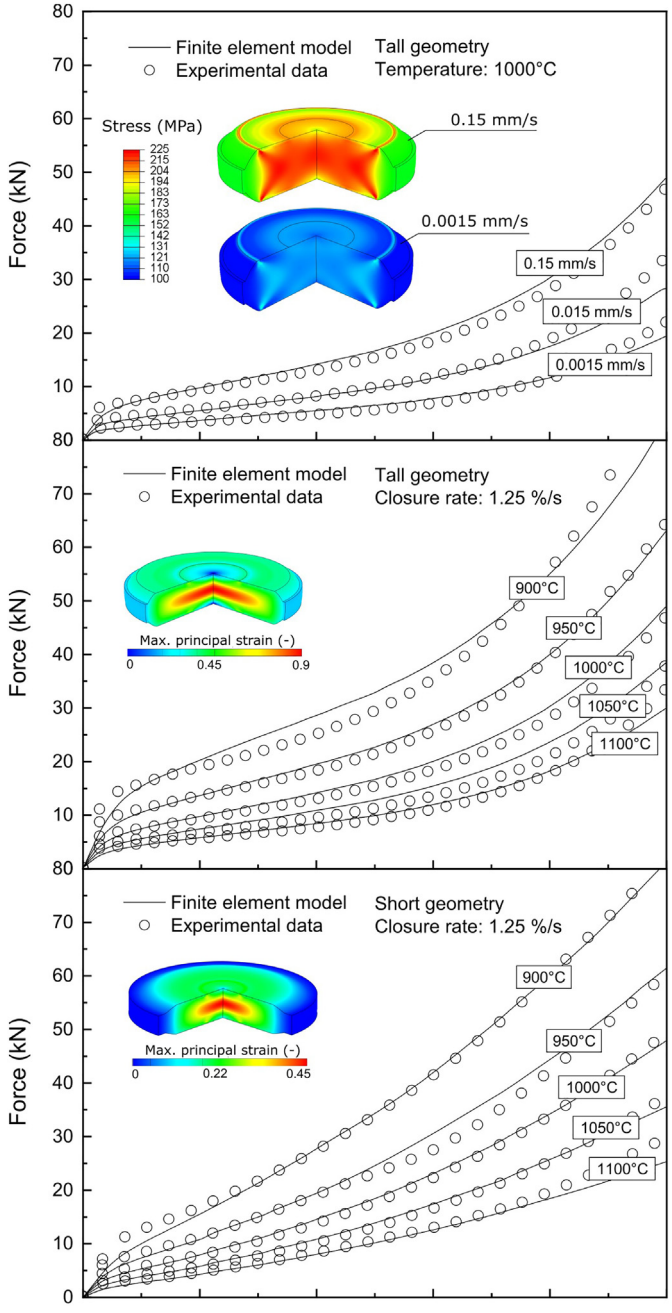

Fig. 17. Experimental vs. predicted load-displacement curves for: top) tests at different displacement rates and constant temperature of 1000 °C and centre/bottom) tests at different temperatures between 900 and 1100 °C and constant displacement rate of 0.15 mm/s for high and low aspect-ratio.

5.2. Effect of temperature on forging behaviour and microstructural evolution

Fig. 14 (a) shows the behaviour of the tall double-cone samples at five different temperatures and a constant displacement rate of 0.15 mm/s. At the tested temperature, only the experiment at 900 °C reached the maximum load before achieving the final displacement. Curves show a strong dependence of the force with the testing temperature. Analogously, Fig. 14 (b) shows the force-displacement behaviour of the short double-cone specimens at five different temperatures at a displacement rate of 0.068 mm/s. In this case, since the height of the specimen is smaller, the strain ranges experienced by the material are smaller too. However, the short geometry also causes the load to increase more rapidly due to the effective area increasing more rapidly. These curves can then be analysed to give an estimate value of the apparent activation energy. Using an Arrhenius relationship, the value of strain rate can be written as a function of the steady-state stress introduced in Eq. (1). By rearranging and simplifying the terms of the equation, the activation energy can be estimated by the slope of the data when plotted as $1/(T)$vs$ln(F^n)$ where F is the measured force for a given displacement and $n = 5$ is the stress exponent as derived previously. Following this, Fig. 15 shows a series of points obtained at different strains or displacement points. The curves of each displacement condition are found to be rather parallel with small differences in slope between them. This plot suggests that there is a unique operating mechanism between 900 and 1100 °C with an apparent activation energy of ≈ 500 kJ/mol — this value is also in agreement with the value measured using isothermal compression tests.

5.3. Validation of the constitutive model

Experimental results obtained from double-cone experimentation are used here to validate the material model. The double-cone experiment was modelled using the finite element method (FEM) in order to compare directly the experimental loads to the reaction forces predicted in the simulation. For this purpose, two-dimensional axisymmetric CAX4T elements were used to model both the dies and the double-cone specimens. Frictional boundary conditions using the general Coulomb friction formulation were employed: these define the minimum shear stress τ_{crit} at which sliding of the surface starts as a function of the contact pressure between the surfaces, thus $\tau_{crit} = \mu p$. A friction coefficient $\mu = 0.2$ was used [40]. Reference points were used to impose the displacement to the die-rods but also to extract the reaction loads. The distribution of strain at different points during the simulation are illustrated in Fig. 16. Fig. 17 compares the simulated and experimental displacement-load curves for both geometries at different temperatures and displacement rates. Comparison shows a good agreement and provides confidence on the proposed constitutive model — it accurately captures the temperature and strain-rate dependency of the underlying mechanisms independently of the forging geometry employed.

The microstructural analysis of the double cone specimens (tall geometry) tested at 900 °C, 1000 °C and 1100 °C is presented in Fig. 18. As with the compression experiments, one can observe a change from a non-recrystallised microstructure of elongated grains at 900 °C to a fully recrystallised microstructure with a refined equiaxed grains at 1000 °C. At higher temperatures (1100 °C), grain growth becomes dominant. The computed distribution of mean grain sizes are also presented in Fig. 18 for each one of those temperatures. It can be observed that the spatial variations of the grain size within the specimen are captured with a good degree of accuracy — a larger mean grain size is reported as the radius of the double-cone increases. The mean grain size trend between different temperatures is also captured: simulations show an initial refinement of the grain size due to recrystallisation at 1000 °C followed by a strong grain growth at 1100 °C.

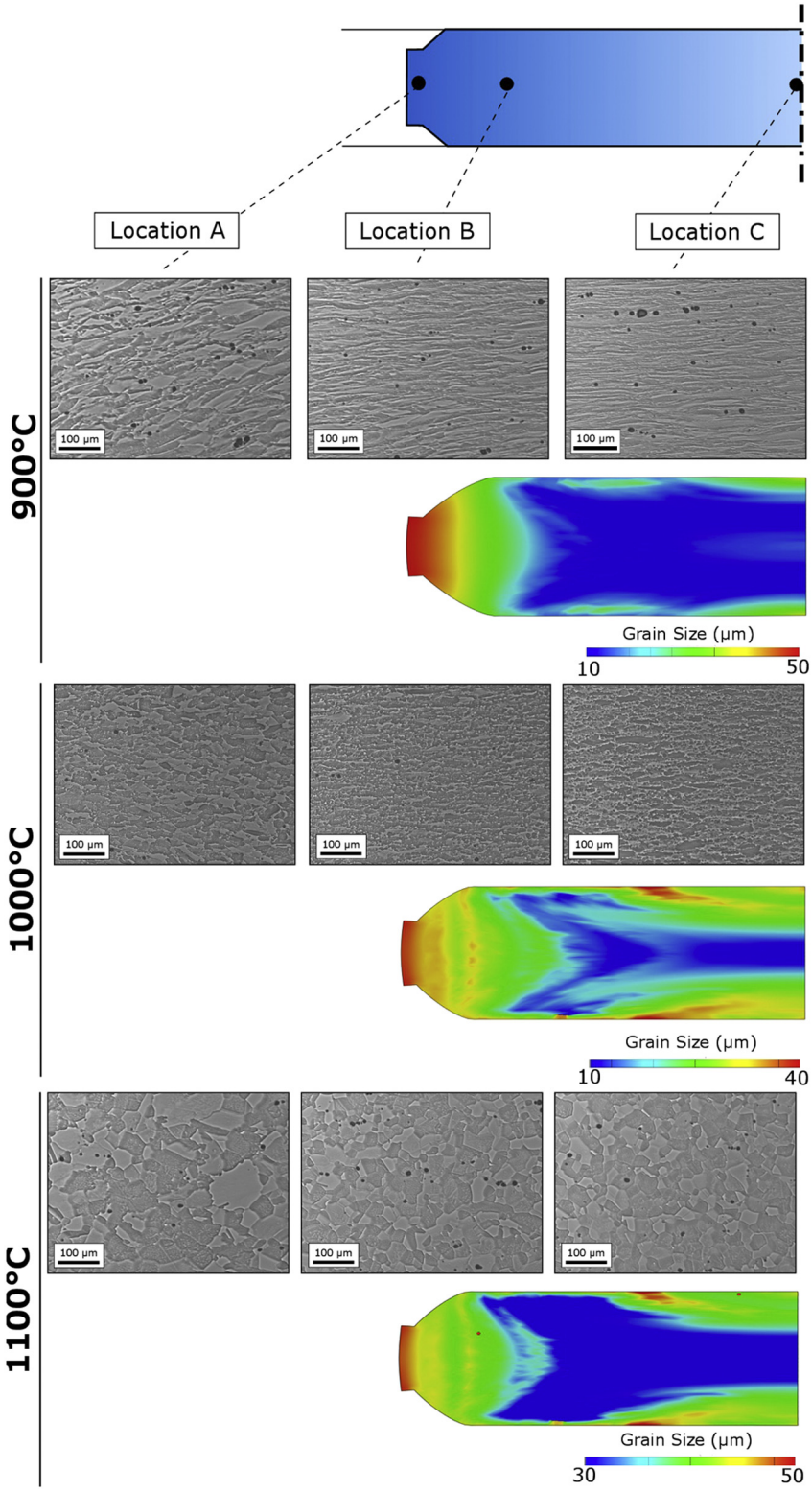

Fig. 18. Experimental optical micrographies and computed mean grain size values of the high aspect-ratio double cone specimens after testing at three different temperatures (900, 1000 and 1100 °C). The micrographies correspond to three different radial positions of the specimen: center, edge of the specimen and approximately 1/4 of the radius of the specimen.

5.4. Application: process modelling of closed-die forging

Having unified constitutive models that accurately capture this temperature and strain-rate dependency of the alloys is critical for the industrial optimisation of manufacturing processes. Particularly, because during hot deformation processes, the forged samples and the dies used to form the metal stock are not necessarily at the same temperature: *e.g.*, the melt stock may change its temperature during forging. For this reason, two different applications of our models were considered here: (i) an isothermal disc forging process — where the temperature was assumed unmutable, and (ii) a coupled stress-temperature analysis — where heat transfer between

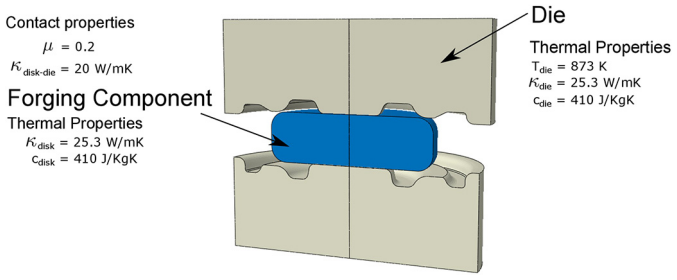

Fig. 19. Diagram of the FEM model used for the simulation of the disc forging process. The thermal and mechanical parameters used for the heat transfer problem are detailed for the die and the disc [23,40].

dies and stock was allowed. The heat transfer parameters are presented in Fig. 19 — these were obtained from values in the literature [23,40]. For the sake of simplicity, the same thermal properties were used in die and disc [41]. The die was discretised as a perfect solid, thus deformation was restricted to the disc exclusively. In order to obtain reliable contact convergence, enough elements were used to assure a smooth surface. Nevertheless, its density should be below that of the slave surface to achieve good convergence of the contact algorithms. Due to the large expected strains – and distortion – experienced by the disc during forging, adaptive remeshing was used in Abaqus/Standard [36]. The same friction law described in the previous section was employed. The disc was meshed with 10,320 CAX4T type elements with distortion and hourglass enhanced controls activated.

Several manufacturing cycles were simulated with different thermal scenarios: (i) isothermal conditions and (ii) forgings where the temperatures of the dies and the metal stock were different and thermal conduction was allowed. The overarching goal was to demonstrate the flexibility of the numerical simulation when dealing with different manufacturing cases and to highlight the importance of a temperature-dependent constitutive model. Processing parameters and geometries presented in this section are believed representative of a turbine disc forging process [23].

The predicted temperature distributions across the disc for the conductive problem of a typical manufacturing cycle are presented in Fig. 20 (a) at three different time-points: (a1) at t =1/3 of the forming process, (a2) at t =2/3 of the forming process, and (a3) at the end of the process. The comparative study of the stress distribution between the isothermal and the non-isothermal cases is presented in Fig. 20 (b) for the three different time points. As the die in contact with the disc reduces the temperature of the metal, the material strengthens and stress concentrations begin to appear. This effect is more pronounced when temperature effects are considered — the regions where temperature is reduced are less prone for plastic deformation. The implications of these stress concentration sites are of vital importance — these regions are linked to surface cracking of the forged components [42]. Fig. 20 (c) shows the grain size evolution along the forging process for each one of the thermal scenarios. These illustrate the importance of having microstructural dependent models which capture its evolution as a function of temperature and strain. One can see that since the strain distribution – and the temperature in the case of non-isothermal forging – is not constant, the mean grain size at the end of the forging process is highly heterogeneous. This microstructural inhomogeneity can introduce important differences in the mechanical performance at different sites in the disc. Having models that can predict their formation and inform for better process design offers substantial engineering advantages for the optimisation of the forging process.

Indeed, in the aerospace industry, there is a significant pressure to reduce the temperature and the manufacturing time for both economical and ecological reasons. The developed model can be used to make critical decisions regarding the optimisation and design of forging processes — with strong potential benefits in both the technical and economical engineering side. For example: (i) forming at lower temperatures increases tool life, reduces surface oxidation, and avoids concurrent grain growth; while (ii) forming at higher strain-rates increases productivity and reduces energy consumption. As an example, Fig. 21 shows the computed required maximum force of the forging case studied here as a function of temperature and the total forging time. This kind of approach can be used to find the most optimal set of forging parameters for a given set of requirements or manufacturing limitations.

Therefore, the framework here proposed shows a simple and rapid methodology for obtaining important information about the

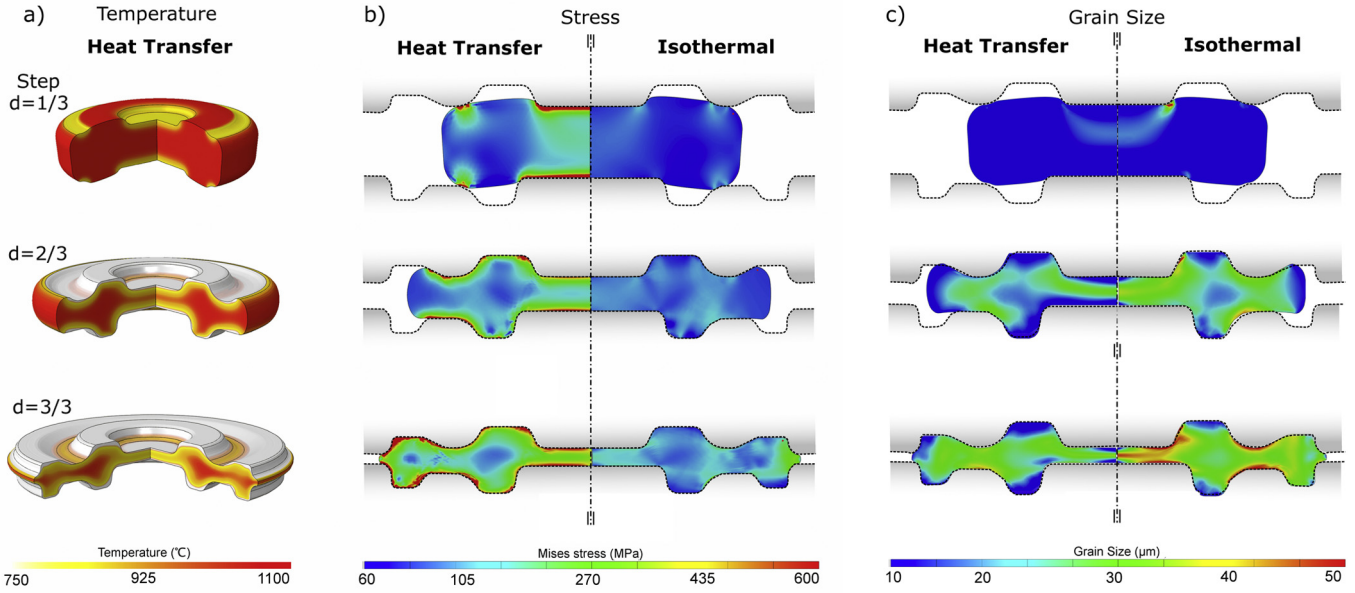

Fig. 20. a)Temperature distribution as a function of forging cycle completion for the heat transfer problem and comparison of the stress distributions (b) and mean grain size (c) between the athermal case and heat transfer case (right).

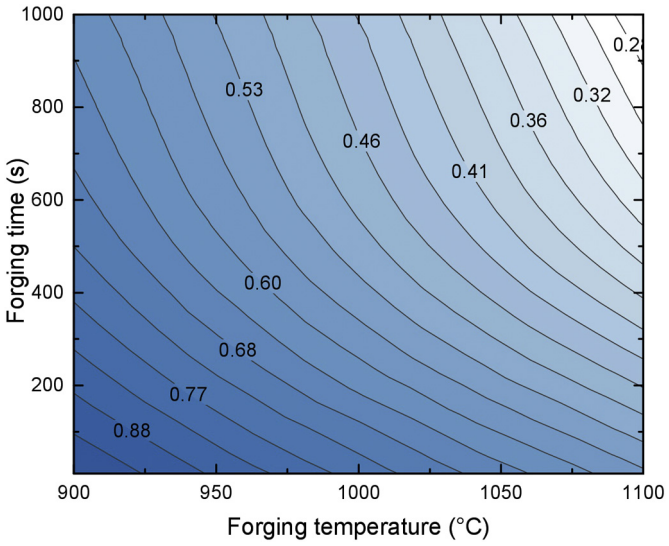

Fig. 21. Contour map showing the maximum die force (in MN) during the forging process as a function of the overall forging time and the forging temperature. Limitation of the forging force leads to a optimum combination of temperature and forging duration.

material behaviour employing a handful of experiments which are representative of forging conditions and which contain enough information regarding the critical microstructural events that typically arise during the high-temperature forging of nickel-based superalloys. Amongst others, it has been shown that this information can be used to find optimal processing parameters which allows engineers to manufacture right-first-time components that meet strength and microstructural requirements while shortening the design process itself.

6. Summary and conclusions

The following conclusions can be drawn from this work:

1. The mechanical response of IN903 has been characterised using isothermal uniaxial compression tests. Experiments reveal a significant dependence on the rate of deformation and the forming temperature. Microstructural assessment describes changes in terms of texture and grain size which arose during deformation.
2. With the above, a viscoplastic model is formulated to describe the constitutive response of the material. The model is usable over the whole range of temperatures and strain rates experimented and appropriately relates microstructural changes to the strain-path behaviour.
3. Double-cone experiments validate the constitutive model. Models capture the loading response both as a function of the temperature and the strain rate. Moreover, rheological analyses reveal consistent values of activation energy and strain rate sensitivity, thus inspiring confidence on the developed framework to extract meaningful information of the underlying mechanisms.
4. The constitutive framework is employed to simulate the forging process of a turbine disc. The model offers a useful tool for process design and optimisation. Moreover, the model reveals the microstructural inhomogeneities which may arise — these can have an impact on the service performance of the component.

Author contribution

Enrique Alabort and Daniel Barba have performed the mechanical tests, characterisation and simulation on a 50/50% basis. Roger Reed has reviewed the article, given advice, and proposed some of the experiments and simulations performed.

References

[1] J.W. Brooks, Forging of superalloys, Mater. Des. 21 (2000) 297–303.
[2] Y.-C. Ho, F.-K. Chen, S. Torng, A study on forging of aluminum-based metal matrix composites, Int. J. Mater. Form. 3 (2010) 351–354.
[3] T. Altan, Forging, Springer Netherlands, Dordrecht, 1986, 157–197.
[4] J. Beddoes, M.J. Bibby, No title, Principles of Metal Manufacturing Processes, Butterworth-Heinemann, Oxford, 1999.
[5] T.F. Azevedo, C.E.C. de Andrade, S.V. dos Santos, A.S. Silva, S. Griza, Fatigue and corrosion-fatigue strength of hot rolled Ti35Nb2.5Sn alloy, Mater. Des. 85 (2015) 607–612.
[6] S. Gardner, W. Li, M. Coleman, R. Johnston, The effects of thermomechanical history on the microstructure of a nickel-base superalloy during forging, Mater. Sci. Eng. A 668 (2016) 263–270.
[7] G. Garces, A. Müller, E. Oñorbe, P. Pérez, P. Adeva, Effect of hot forging on the microstructure and mechanical properties of Mg-Zn-Y alloy, J. Mater. Process. Technol. 206 (2008) 99–105.
[8] F.C. Ma, W.J. Lu, J.N. Qin, D. Zhang, The effect of forging on microstructure and mechanical properties of in-situ TiC/Ti composite, Mater. Trans. 47 (2006) 1322–1327.
[9] X.M. Chen, Y.C. Lin, D.X. Wen, J.L. Zhang, M. He, Dynamic recrystallization behavior of a typical nickel-based superalloy during hot deformation, Mater. Des. 57 (2014) 568–577.
[10] Y. Estrin, L. Toth, A. Molinari, Y. Brechet, A dislocation-based model for all hardening stages in large strain deformation, Acta Mater. 46 (1998) 5509–5522.
[11] R. Liu, M. Salahshoor, S.N. Melkote, T. Marusich, A unified internal state variable material model for inelastic deformation and microstructure evolution in SS304, Mater. Sci. Eng. A 594 (2014) 352–363.
[12] A.A. Brown, D.J. Bammann, Validation of a model for static and dynamic recrystallization in metals, Int. J. Plast. 32–33 (2012) 17–35.
[13] L.A. Reyes, P. Páramo, A. Salas Zamarripa, M. de la Garza, M.P. Guerrero–Mata, Influence of processing parameters on grain size evolution of a forged superalloy, J. Mater. Eng. Perform. 25 (2016) 179–187.
[14] M.F. Horstemeyer, D.J. Bammann, Historical review of internal state variable theory for inelasticity, Int. J. Plast. 26 (2010) 1310–1334.
[15] C. Roucoules, M. Pietrzyk, P.D. Hodgson, Analysis of work hardening and recrystallization during the hot working of steel using a statistically based internal variable model, Mater. Sci. Eng. A 339 (2003) 1–9.
[16] P. Mignanelli, N. Jones, K. Perkins, M. Hardy, H. Stone, Microstructural evolution of a delta containing nickel-base superalloy during heat treatment and isothermal forging, Mater. Sci. Eng. A 621 (2015) 265–271.
[17] G.-z. Quan, J. Pan, X. Wang, Z.-h. Zhang, L. Zhang, T. Wang, Correspondence between grain refinements and flow softening behaviors at Nimonic 80A superalloy under different strain rates, temperatures and strains, Mater. Sci. Eng. A 679 (2017) 358–371.
[18] K.K. Li, M.S. Chen, Y.C. Lin, W.Q. Yuan, Microstructural evolution of an aged Ni-based superalloy under two-stage hot compression with different strain rates, Mater. Des. 111 (2016) 344–352.
[19] N.R. Moody, R.E. Stoltz, M.W. Perra, The effect of hydrogen on fracture toughness of the Fe-Ni-Co superalloy IN903, Metall. Trans. A. 18 (1987) 1469–1482.
[20] E. Alabort, D. Putman, R. Reed, Superplasticity in Ti-6Al-4V: characterisation, modelling and applications, Acta Mater. 95 (2015) 428–442.
[21] L. Tan, Z. Huang, F. Liu, G. He, X. Wang, L. Huang, Y. Zhang, L. Jiang, Effects of strain amount and strain rate on grain structure of a novel high Co nickel-based polycrystalline superalloy, Mater. Des. 131 (2017) 60–68.
[22] J. Lin, Y. Liu, A set of unified constitutive equations for modelling microstructure evolution in hot deformation, J. Mater. Process. Technol. 143–144 (2003) 281–285.
[23] Q. Bai, J. Lin, J. Jiang, T. Dean, J. Zou, G. Tian, A study of direct forging process for powder superalloys, Mater. Sci. Eng. A 621 (2015) 68–75.
[24] J.-P. Thomas, E. Bauchet, C. Dumont, F. Montheillet, EBSD investigation and modeling of the microstructural evolutions of superalloy 718 during hot deformation, Proceedings of superalloys, 2004, pp. 959–968.
[25] T. Ma, M. Yan, X. Yang, W. Li, Y. Chao, Microstructure evolution in a single crystal nickel-based superalloy joint by linear friction welding, Mater. Des. 85 (2015) 613–617.
[26] Y.C. Lin, D.-X. Wen, M.-S. Chen, X.-M. Chen, A novel unified dislocation density-based model for hot deformation behavior of a nickel-based superalloy under dynamic recrystallization conditions, Appl. Phys. A 122 (2016) 805.
[27] S. Roy, S. Suwas, The influence of temperature and strain rate on the deformation response and microstructural evolution during hot compression of a titanium alloy Ti-6Al-4V-0.1B, J. Alloys Compd. 548 (2013) 110–125.
[28] X. Tang, B. Wang, Y. Huo, W. Ma, J. Zhou, H. Ji, X. Fu, Unified modeling of flow behavior and microstructure evolution in hot forming of a Ni-based superalloy, Mater. Sci. Eng. A 662 (2016) 54–64.

[29] Y.C. Lin, X.M. Chen, D.X. Wen, M.S. Chen, A physically-based constitutive model for a typical nickel-based superalloy, Comput. Mater. Sci. 83 (2014) 282–289.
[30] http://www.specialmetals.com/tech-center/alloys.html.
[31] H. Mecking, U. Kocks, Kinetics of flow and strain-hardening, Acta Metall. 29 (1981) 1865–1875.
[32] J. Lin, Y. Liu, D. Farrugia, M. Zhou, Development of dislocation-based unified material model for simulating microstructure evolution in multipass hot rolling, Philos. Mag. 85 (2005) 1967–1987.
[33] R. Ding, Z. Guo, Coupled quantitative simulation of microstructural evolution and plastic flow during dynamic recrystallization, Acta Mater. 49 (2001) 3163–3175.
[34] Y. Estrin, Dislocation theory based constitutive modelling: foundations and applications, J. Mater. Process. Technol. 80-81 (1998) 33–39.
[35] J. Cao, J. Lin, A study on formulation of objective functions for determining material models, Int. J. Mech. Sci. 50 (2008) 193–204.
[36] Abaqus Implicit, Dassault Systémes. 2010.
[37] F. Dunne, N. Petrinic, Introduction to Computational Plasticity, Oxford University Press, USA, 2005.
[38] D. Barba, E. Alabort, D. Garcia-Gonzalez, J.J. Moverare, R.C. Reed, A. Jérusalem, A thermodynamically consistent constitutive model for diffusion-assisted plasticity in Ni-based superalloys, Int. J. Plast. 105 (2018) 74–98.
[39] E. Alabort, D. Barba, S. Sulzer, M. Lißner, N. Petrinic, R. Reed, Grain boundary properties of a nickel-based superalloy: characterisation and modelling, Acta Mater. 151 (2018).
[40] W.L. Zhou, W.H. Chen, F.J. Zhang, Forming process simulation and optimization of nickel-base superalloy turbine disk, Adv. Mater. Technol. 1004 (2014) 1156–1161.
[41] A. Loyda, G.M. Hernández-Muñoz, L.A. Reyes, P. Zambrano-Robledo, Microstructure modeling of a Ni-Fe-based superalloy during the rotary forging process, J. Mater. Eng. Perform. 25 (2016) 2128–2137.
[42] H. Kakimoto, T. Arikawa, Prediction of surface crack in hot forging by numerical simulation, Proc. Eng. 81 (2014) 474–479.